



Università degli Studi Mediterranea di Reggio Calabria
Archivio Istituzionale dei prodotti della ricerca

Chemical Vapor Deposited Graphene-Based Derivative As High-Performance Hole Transport Material for Organic Photovoltaics

This is the peer reviewed version of the following article:

Original

Chemical Vapor Deposited Graphene-Based Derivative As High-Performance Hole Transport Material for Organic Photovoltaics / Capasso, A; Salamandra, L; Faggio, Giuliana; Dikonimos, T; Buonocore, F; Morandi, V; Ortolani, L; Lisi, N. - In: ACS APPLIED MATERIALS & INTERFACES. - ISSN 1944-8244. - 8:36(2016), pp. 23844-23853. [10.1021/acsami.6b06749]

Availability:

This version is available at: <https://hdl.handle.net/20.500.12318/3408> since: 2020-12-20T19:10:17Z

Published

DOI: <http://doi.org/10.1021/acsami.6b06749>

The final published version is available online at: <https://pubs.acs.org/doi/10.1021/acsami.6b06749>

Terms of use:

The terms and conditions for the reuse of this version of the manuscript are specified in the publishing policy. For all terms of use and more information see the publisher's website

Publisher copyright

This item was downloaded from IRIS Università Mediterranea di Reggio Calabria (<https://iris.unirc.it/>) When citing, please refer to the published version.

(Article begins on next page)

Chemical vapor deposited graphene-based derivative as high-performance hole transport material for organic photovoltaics

Andrea Capasso^{†,}, Luigi Salamandra^{‡,§}, Giuliana Faggio[‡], Theodoros Dikonimos[†], Francesco Buonocore[†], Vittorio Morandi[§], Luca Ortolan[§], Nicola Lisi[†]*

[†]ENEA, Laboratorio Materiali e Processi Fisico-Chimici, Casaccia Research Centre, Via
Anguillarese 301, Rome, 00060, Italy

^{*}Istituto Italiano di Tecnologia, Graphene Labs, Via Morego 30, Genova, 16163, Italy

[‡]Istituto Superiore delle Comunicazioni e delle Tecnologie dell'Informazione (ISCOM),
Ministero dello Sviluppo Economico, Viale America 201, Rome, 00144, Italy

[§]Department of Electronic Engineering, University of Rome "Tor Vergata", Via del Politecnico
1, Rome, 00133, Italy

[‡]Dipartimento di Ingegneria dell'Informazione, delle Infrastrutture e dell'Energia Sostenibile
(DIIES), Università "Mediterranea" di Reggio Calabria, Reggio Calabria, 89122, Italy

[§]CNR-IMM Bologna, Via Gobetti, 101, Bologna, 40129, Italy

KEYWORDS: organic photovoltaics, hole transport layer, functionalized graphene film, graphene-based derivative, ethanol CVD.

ABSTRACT. The development of efficient charge transport layers is a key requirement for the fabrication of efficient and stable organic solar cells. A graphene-based derivative with planar resistivity exceeding $10^5 \Omega/\square$ and work function of 4.9 eV is here produced by finely tuning the parameters of the chemical vapor deposition process on copper. After the growth, the film is transferred on glass/indium tin oxide and used as hole transport layer in organic solar cells based on a PBDTTT-C-T:[70]PCBM blend. The cells attained a maximum power conversion efficiency of 5%, matching reference cells made with state-of-the-art PEDOT:PSS as the hole transport layer. Our results indicate that functionalized graphene represents an effective alternative to PEDOT:PSS as hole transport/electron blocking layer in solution-processed organic photovoltaics.

1. INTRODUCTION

The research on renewable energy sources continues to attract considerable effort and funding, a situation motivated by the steady increase in the cost related to the exploitation of “classic” fossil sources, both from the environmental and economic point of view.¹⁻² Harvesting energy from fossil fuels is intrinsically unsustainable in a sufficiently long time-frame because of both the limited availability of resources and the massive impact on the environment. In this context, solar energy is an unlimited source of power. Silicon photovoltaic cells have demonstrated the ability to generate a large fraction of the electric grid power at costs competitive with fossil fuels.³ Organic solar cells (OSCs) represent an alternative photovoltaic technology that has been intensively pursued in the last decades. These cells are capable of a lower power conversion

efficiency than single crystal silicon ones (the current records being 11.7% vs 25% [<http://www.nrel.gov/ncpv/>]), but present low production cost and entail small environmental impact.⁴ OSCs cells can be fabricated by simple, mass-production techniques, such as coating or printing, using inexpensive and readily-available materials (*e.g.*, polymers and fullerene derivatives).⁵⁻⁷ In this way, flexible and lightweight devices can be produced, even on large scale by techniques such as roll-to-roll printing.⁸⁻⁹ Flexible devices have an energy pay-back time of a few days and can be installed in context precluded to heavy and rigid silicon-based devices.^{2, 10} Recently, this technology made progress also in terms of maximum achievable power conversion efficiency (η), with several groups reporting values beyond 11%.¹¹⁻¹³ Typically, an active layer made blending a p-type polymer with a n-type fullerene derivative is inserted between two electrodes, a metal and a transparent conductive oxide (TCO), interfacing them with buffer layers working as hole- (HTL) or electron-transport layers (ETL).¹⁴ The η can be further enhanced by using a tandem architecture, in which two or more active layers (subcells) with complementary absorption spectra (ideally matching the entire solar spectrum) are sandwiched together, in conjunction with appropriate buffer materials at the layer interfaces.¹⁵

Although the active layer is the core of any OPV device, the cell performance is strongly affected by the presence of selective HTL and ETL buffer layers, added between the active layers and each electrode to favor the charge separation and ease the charge carriers flow. The discovery, development and tuning of stable selective transport layers is thus mandatory for the future success of OPV technology. The HTL is usually deposited on top of the indium tin oxide (ITO) conductive electrode to selectively collect holes while blocking the electron flow, thus minimizing current leakage due to charge recombination. Many materials were proposed to fabricate the HTL. Wide band gap p-type semiconductors possess in principle the required

characteristics, and thin layers (usually no more than 50 nm) of metal oxides such as NiO, MoO₃, WO₃, V₂O₅¹⁶ have been deposited by thermal evaporation as HTL, allowing good cell performances. All such layers offered high transparency in the visible range and favorable energy levels (*i.e.*, valence band maximum) for efficient hole collection; however, vacuum deposition techniques such evaporation are both too expensive and incompatible with solution processing fabrication. PEDOT:PSS is currently the most widely used HTL for OPV. This material has an appropriate work function value for the collection of holes from the HOMO level of the polymers (in the range 5.0-5.3 eV)¹⁷ and can be easily processed in water. When deposited it also helps to flatten the rough ITO surface, improving the electric contact between active layer and anode. As a downside, PEDOT:PSS is highly acidic and might corrode the ITO electrode, decreasing the overall performance of the devices.¹⁸

Graphene is a monolayer material possessing exceptional optical, electrical, mechanical properties. Being composed of a single atomic layer, this material can be readily functionalized by selectively breaking its C=C double bonds (even at specific, selected locations), which can be then saturated with heterogeneous functional groups. In this way, graphene-based derivatives (GBD) with different properties can be created. Graphane¹⁹ and fluoro-graphene²⁰ are examples of periodic and crystalline GBDs: the former is a fully hydrogenated graphene, while the latter is a fluorinated derivative. Another example is graphene oxide (GO), whose structure (as observed so far) is amorphous or inhomogeneous, and containing a mix of sp²/sp³ carbon.²¹ The possibility of producing GBDs with desired properties to function as interfacial, buffer or active layers offer an unprecedented opportunity for photovoltaics.^{4, 22-30} Solution-processed GO was the first GBD to be efficiently used as HTL in OSCs.³¹ Although an optimal band alignment with the polymer HOMO was reached, the thickness resulted a critical issue: the GO layer had to be not more than

2nm-thick to avoid significant reduction in the cell fill factor and η .^{26, 32} Usually, GBDs are prepared by processing pristine graphene (produced by mechanical exfoliation³¹ or thermal CVD¹⁹⁻²⁰) to alter its lattice and add the required functional groups. In the case of hydrogenated graphene, the growth by plasma enhanced CVD at 600°C was also reported.³³

In the present study we focus on the direct growth of a GBD by thermal catalytic CVD in a range of temperature whose thermodynamic conditions favor the insertion of functional groups in the forming lattice. Our previous work showed that by varying the CVD temperature from 1070°C to 930°C with ethanol as carbon precursor and copper foils as growth substrate, it is possible to modify the composition and structure of the carbonaceous film, ultimately determining its sheet resistance (increasing from 0.5 to 4.3 k Ω /sq when lowering the CVD temperature from 1070 to 930°C).³⁴ Similar studies (with ethanol as precursor and on copper as catalyst) reported that a CVD temperature of 900°C leads to the growth of a functionalized GBD comprising oxygen-containing groups coordinated in the carbon lattice, which affect the electrical properties of the film (as confirmed by XPS analysis showing an increase fraction of sp³ bound atoms in the C1s peak).³⁵ When using ethylene as growth precursor at low temperature (down to 800°C), films with high resistivity (in comparison to pristine graphene) were also reported, but in this case the such electrical behavior was rather attributed the to the insurgence of nano-crystalline domains in the films, as suggested by the smaller L_a values derived by the Raman spectra.³⁶⁻³⁷

Herein, we purposely explored a wide temperature range (600-1070°C) for ethanol-CVD on copper in order to systematically alter the sp²/sp³ ratio of the GBD carbon lattice. By adjusting the growth temperature and selecting appropriate CVD conditions, we tuned the GBD properties to render it efficient as hole transport layer in organic solar cells. Namely, with a CVD process at

790°C we created a monolayer GBD with planar resistivity beyond $10^5 \Omega/\square$ and work function of 4.9 eV. We performed a wide set of structural, compositional, electrical analyses on the GBD to determine its structure and electronic properties. Our results show that the GBD film is composed of a mixed phase of sp^2/sp^3 hybridized carbons lacking oxygen, where the electron transport occurs via charge hopping between localized states (sp^2 sites) at the Fermi level.³² The monoatomic GBD film was transferred on top of ITO substrates to fabricate OSCs with PBDTTT-CT as active layer to be tested as HTL. As comparison, we also fabricated OSCs with pristine graphene grown at 1070°C³⁸ and with commonly-used PEDOT:PSS as HTLs.¹⁸

2. RESULTS AND DISCUSSION

2.1. Materials Characterizations

Figure 1a shows the low-magnification (LM) TEM image of the film grown at 1070°C and deposited on a standard TEM grid. The morphology is typical of graphene films transferred on TEM grids, with large and homogeneous sheets laid over the grid and folded at suspended edges. Figure 1b shows a detail of a folded edge in the region indicated by the arrow in Figure 1a. The high-resolution electron microscopy (HRTEM) image clearly shows graphite (002) fringes (as shown in the inset) where the graphene sheet folds over itself. The count of these fringes at folded edges allows for a precise determination of the number of graphene layers composing the film, and it resulted to be between 1 and a few layers. The regular and straight (002) fringes are indicative of a high degree of lattice perfection in the graphene grown at 1070°C, as confirmed by electron diffraction (ED) (Figure 1c) performed using a selected area aperture corresponding to a diameter of 800 nm, where the typical ring-like reflections from the honeycomb lattice of graphene are observed. The inner ring in Figure 1c corresponds to an inter-planar distance of 0.213 nm, while the outer one corresponds to 0.123 nm, as expected for graphene films.³⁹

Figures 1d-f show TEM data from the GBD grown at 790°C. Irrespective of a CVD temperature lower than that usually required for the synthesis of standard graphene, the film shown in the micrographs has a regular structure and is composed of a single layer, with defined, clean and straight edges. Figure 1d shows the LM TEM image of the synthesized film over the TEM grid. In the regions of the sample where folding occurred (like the one indicated by the white rectangle in Figure 1d and observed at higher magnification in Figure 1e) it has been possible to count the number of layers composing the film, which resulted to be between 1 and 4 for the whole film over the grid. Despite the lower synthesis temperature, by analyzing the lattice fringes in the HREM image it emerges that the film has a high crystalline quality, as confirmed by the electron diffraction (ED) examination. Figure 1f displays a typical ED pattern acquired from the sample, using a selected area aperture corresponding to a diameter of 150 nm, showing sharp ring-like reflections from poly-crystalline hexagonal honeycomb lattice. The outer ring spacing is of 0.12 nm, corresponding to a small contraction of the lattice parameter by ~5%, which is comparable with the experimental error. From these TEM results, it can be stated that the GBD grown at 790°C is a polycrystalline carbonaceous film, a few to a single layer thick.

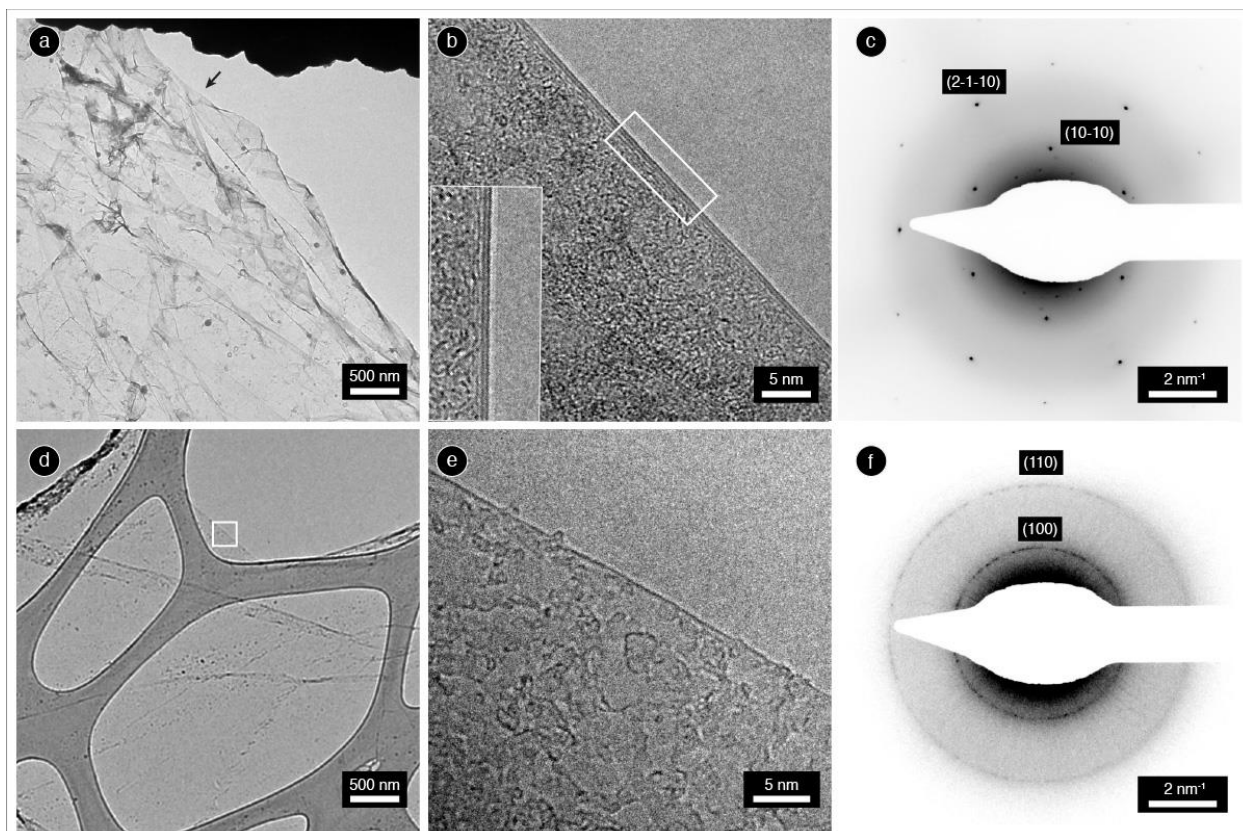


Figure 1 – TEM analysis of the graphene (grown at 1070°C, panels a-c) and GBD (grown at 790°C, panels d-f) films. a) LM image of the graphene film. b) High-resolution image of a folded edge indicated by the arrow in a), and detail of the (002) graphite fringes at the border. c) ED pattern from an area of 800 nm of diameter, showing hexagonal reflections from the honeycomb lattice of graphene layers. d) LM image of the GBD film on the holey carbon film of the TEM grid. e) Detail of a folded edge of the film, from the region in the white rectangle in panel d. f) ED pattern from an area of 150 nm of diameter, showing 9 hexagonal patterns from the honeycomb lattice of the film.

The graphene and GBD films were investigated by Raman spectroscopy after transfer onto Si/SiO₂ (300 nm). On account of possible local inhomogeneity in the sample surface, the averaged spectra are shown for each sample. In the two spectra (Figure 2) the main features

typical of graphene appear: the G peak (at $\sim 1580\text{ cm}^{-1}$) due to the in-plane bond- stretching of all pairs of sp^2 -carbon atoms in both rings and chains, the D peak (at $\sim 1350\text{ cm}^{-1}$) due to a breathing mode of six-atom rings and requiring disorder or defects for its activation, and the 2D peak at $\sim 2700\text{ cm}^{-1}$ that originates from a double resonance Raman process. The graphene film grown at 1070°C has a negligible D peak, and strong G and 2D peaks with an intensity ratio $I_{2D}/I_G > 3$.⁴⁰ These are the distinctive features of highly crystalline, single-layer graphene.⁴¹ The GBD film grown at 790°C has instead a D peak as the most prominent feature, a G peak much less intense than that of graphene and a very weak 2D peak. Besides, a well-defined peak at $\sim 1620\text{ cm}^{-1}$ (D' peak) appears with an intensity similar to the G peak. This D' peak is connected to disorder as the D peak, but occurring in this case via an intravalley double-resonance process in the presence of defects.⁴²⁻⁴⁴

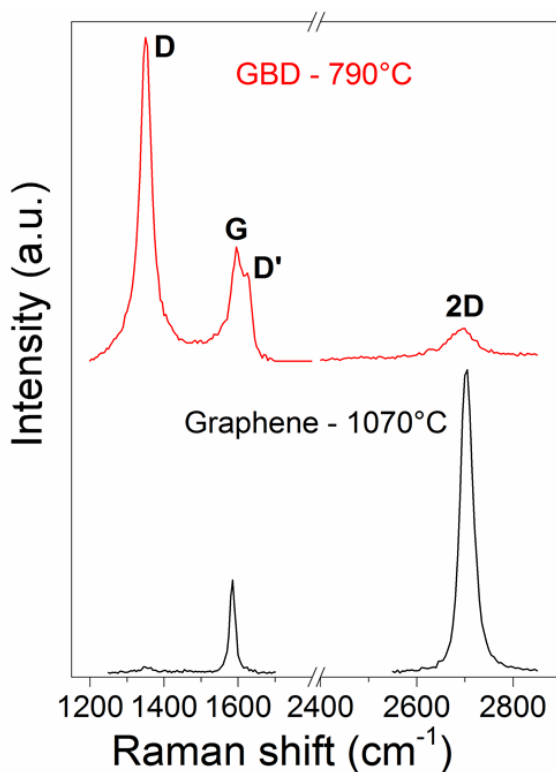


Figure 2 – Raman spectra of the graphene and GBD films.

In Table 1 we compare the values of D, G e 2D, their position (ω) and full width half maximum (Γ). The average inter-defect distance L_d (mean distance between two defects, calculated by integrated area)⁴⁵ is also provided.

Table 1 Relevant parameters derived from the Raman spectra. Indicating with L_d the mean distance between two defect, at low defect concentration (Stage 1) $I_D/I_G \approx 1/L_d$ and at high defect concentration (Stage 2) $I_D/I_G \approx L_d^2$.⁴⁶

		790°C	1070°C
ω (cm^{-1})	D	1350.8	1351.8
	G	1596.4	1584.7
	2D	2691.5	2703.5
Γ (cm^{-1})	D	38.1	21.8
	G	36.6	16.6
	2D	57.5	27.8
I_D/I_G		2.89	0.10
I_{2D}/I_G		0.25	3.37
L_d (nm)		3.29	168.3

Being strictly connected to disorder, the D and D' bands are an excellent indicator of the overall defectiveness of the sp^2 carbon lattice of graphene,³⁷ although it is not straightforward to extract information on the defect type and density from the analysis of the spectrum. By progressively inducing more controlled damage (increasing level of defects by Ar ion bombardment) into crystalline graphene samples (from mechanical exfoliation) some recent studies have identified a two stage scenario:⁴⁷⁻⁴⁹ an initial low defect density “Stage 1” and a high defect density “Stage 2” when the average inter-defect distance falls in the nm range.⁴⁸ These studies demonstrated that the intensity ratio I_D/I_G does not depend on nature of the defect and in contrast, only in the limit of low defect density (Stage 1), the intensity ratio I_D/I_G can be put in relation with the defect type, since vacancies appear to lead to an higher D' than sp^3 bonds.

Such scenario is demonstrated only at low defect density, while it is believed that when the average inter-defect distance falls in the nm range, such analysis ceases to be correct and the information about the defect type is lost.⁴⁷ Since the covalent bonding of functional groups to the graphene plane implies the partial conversion of sp^2 into sp^3 bonds,⁵⁰ which contribute to the overall D feature, these studies are extremely relevant for discriminating among random defectiveness or lattice damage, and controlled functionalization. While the former mostly spoils many of the graphene desirable properties, the latter can modify graphene in many substantial and useful ways.^{19, 50} From the I_D/I_G values and the width of the bands (see Table 1), the GBD film appears not to belong to the low defect regime, or to the Stage 1 type, and therefore we cannot draw conclusions on the defect type. By examining Raman and TEM data it emerges that the I_D/I_G ratio increase cannot be entirely attributed to the occurrence of a carbon film made of small, nm size graphitic crystals,³⁶ since the two-dimensional regular structure emerging from Figure 1f and the diffraction pattern reported in Figure 1e are not compatible with this scenario. By using a spot of 150 nm we counted 9-14 reflections on the 17500 nm² illuminated area, and we can thus estimate an average domain area of 1200-1900 nm², which (assuming a circular shape) leads to a grain diameter of 20-25 nm. The elevated I_D/I_G at low temperature must thus be affected by a contribution linked to the occurrence of covalently bonded functional groups which break and interrupt the sp^2 lattice symmetry with sp^3 carbons, or to the insurgence of a massive quantity of point like defects such as vacancies. In order to rule out this last possibility, the chemical bonding state of the film has been ascertained by XPS. Overall, the Raman and TEM analyses demonstrate that the GBD is not made of nm-sized graphitic domains but rather of a sp^2 carbon lattice with a large amount of carbon-containing groups in sp^3 -coordination.

XPS spectra were collected onto the Cu samples a few minutes after the graphene growth (thus only shortly exposed to air) in order to evaluate the kind of carbon bonding (Figure 3). The peak fitting was carried out taking into account the chemical shift of the main components according to test samples of graphite and CVD diamond and considering literature data.⁵¹⁻⁵³ For the GBD film, the C1s spectrum in Figure 3a shows two main components, representative of sp^2 and sp^3 C bonds.⁵¹ The sp^3 feature is wider with respect to the test diamond (not reported in the graph) and might be assigned to hydrogenated, C-H, carboxyl C-O-H or epoxide C-O-C bonds. Overall, the sp^3 component account to ~40% of the total carbon atoms (~57% for the sp^2 component). X-ray Auger electron spectroscopy (XAES) can give further hints into the carbon film structure.⁵⁴ We calculated the Auger D parameters from the spectra reported in Figure 3b and 3d: 18 eV for the GBD and 22 eV for graphene. This comparison further confirm the presence of a consistent content of sp^3 hybridized carbons in the GBD lattice. Previous work on graphene films grown by ethanol CVD at 900°C³⁵ reported the C1s XPS peak fitted with three Gaussian peaks centered at 284.2 eV, 285.5 V and 288.3 eV, attributed to sp^2 hybridized carbons (C=C), keto (C=O) and sp^3 carboxylic (COOH) or epoxy (C-O-C) groups, respectively. However, the authors provided no information about the oxygen O1s peak (in the region around 532 eV) and did not extended the study to samples grown at temperatures below 800°C.³⁵ In our XPS analysis, we fitted the C1s peak of the GBD grown at 790°C with four components, a sp^2 peak at 284.6 eV, a sp^3 peak at 285.2 eV, a two small peaks at 286.7 and 287.8 eV. No oxygen signal in the O1s region was detected neither in the graphene nor in the GBD films, despite using long acquisition times. The reference spectrum of graphene is reported in Figure 3c, showing a consistently lower level of sp^3 bonds and perfectly overlapping with the spectrum of a test (polycrystalline) graphite sample. The large fraction of sp^3 bonded carbons in the GBD film should be thus assigned to C-H bonds,

since oxidized bonds are excluded due to the lack of oxygen signal. On the contrary, the two peaks at 286.7 and 287.8 eV which emerge from the background are so weak that might be related to a minor component of oxidized bonds possibly coming from air exposure (in this case the oxygen content is so small to be close to the detection limit, estimated to be around 0.1% of the total atom percentage in our XPS system, explaining why no oxygen signal in the O1s peak is revealed).

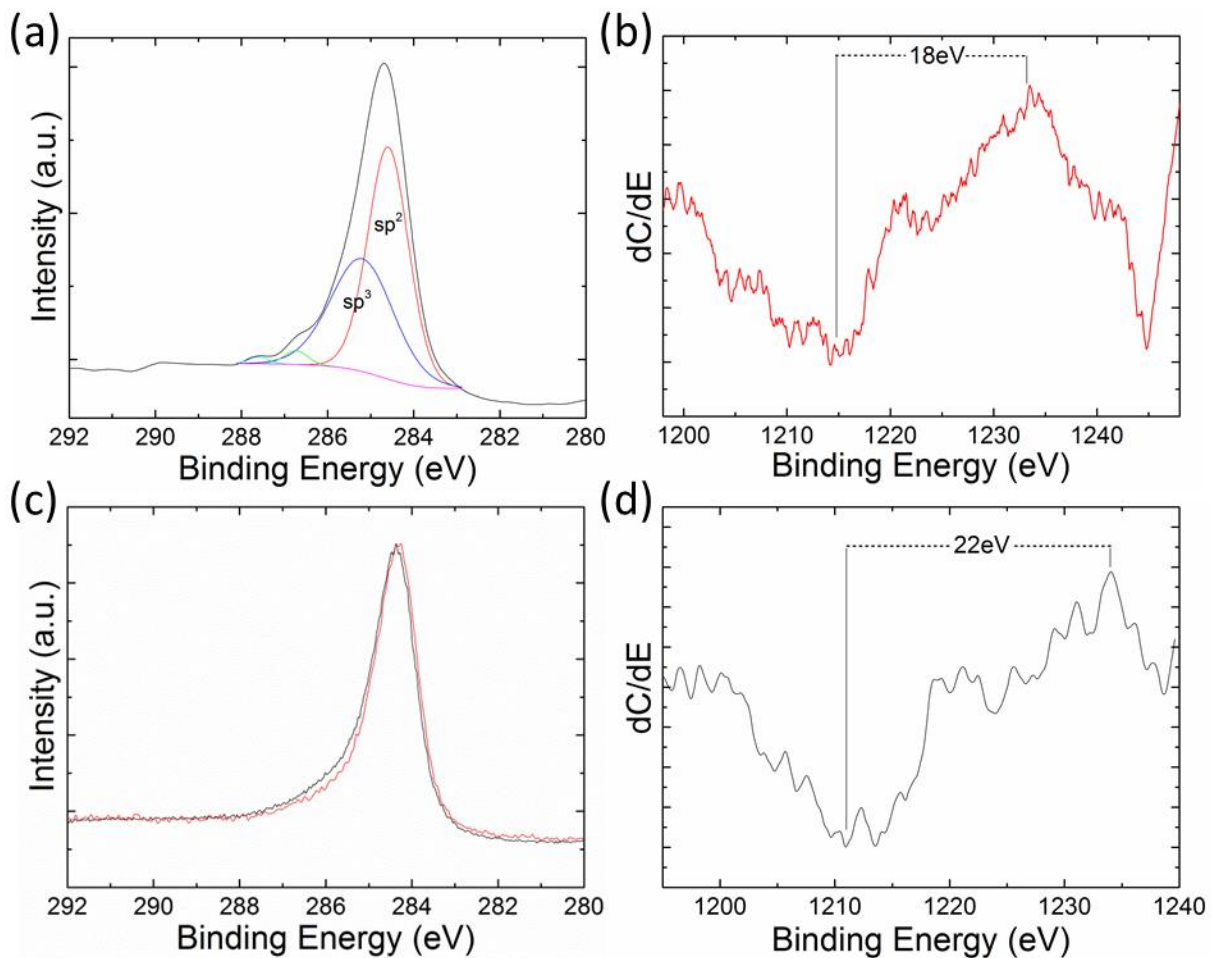


Figure 3 – XPS analysis of the CVD samples. C1s peak of the GDB grown at 790°C (a) and of the graphene grown at 1070°C (c). In (a) the C1s peak fitting is proposed, while in (c) the spectrum is compared to that of a test graphite sample (red curve). The Carbon KLL edge

differential spectrum with measurement of the auger “D parameter” is reported in (b) and (d) for the GBD and graphene, respectively.

After the transfer of the CVD-grown films onto glass/ITO substrates, atomic force and Kelvin probe force microscopy (AFM/KPFM) were performed on glass/ITO and glass/ITO/GBD samples (Figure 4, $25 \mu\text{m}^2$ sample regions) to investigate the topography and surface potential in the two cases. The AFM image of the glass/ITO sample show the typical grains composing the oxide (Figure 4a), while in the case of glass/ITO/GBD a few wrinkles of the GBD film are also visible (Figure 4b). Such wrinkles are routinely found also in graphene films grown at 1070°C .⁴⁴ As for the surface potential of the samples, its variation over the surface is rather smooth, with no sharp steps correlated with topographical features (Figure 4c and d, where histograms of the potential measured over the scanned area is also shown in the insets). To obtain the work function value of the two samples, a highly order pyrolytic graphite (HOPG) crystal of known work function ($\Phi_{\text{HOPG}}=4.65$) was measured, and the tip work function was then calculated to be $\Phi_{\text{tip}}=4.95$ eV. The measured average surface potential values of glass/ITO and glass/ITO/GBD are 200 mV and 30 mV. Therefore, the work function value of glass/ITO is $\Phi_{\text{ITO}}=4.7\pm 0.05$ eV, while that of glass/ITO/GBD is $\Phi_{\text{GBD}}=4.9\pm 0.05$ eV. The work function of glass/ITO/graphene was evaluated for comparison by Kelvin Probe method, finding a $\Phi_{\text{graphene}}\approx 4.6$ eV, in line with the values reported in literature.⁵⁵

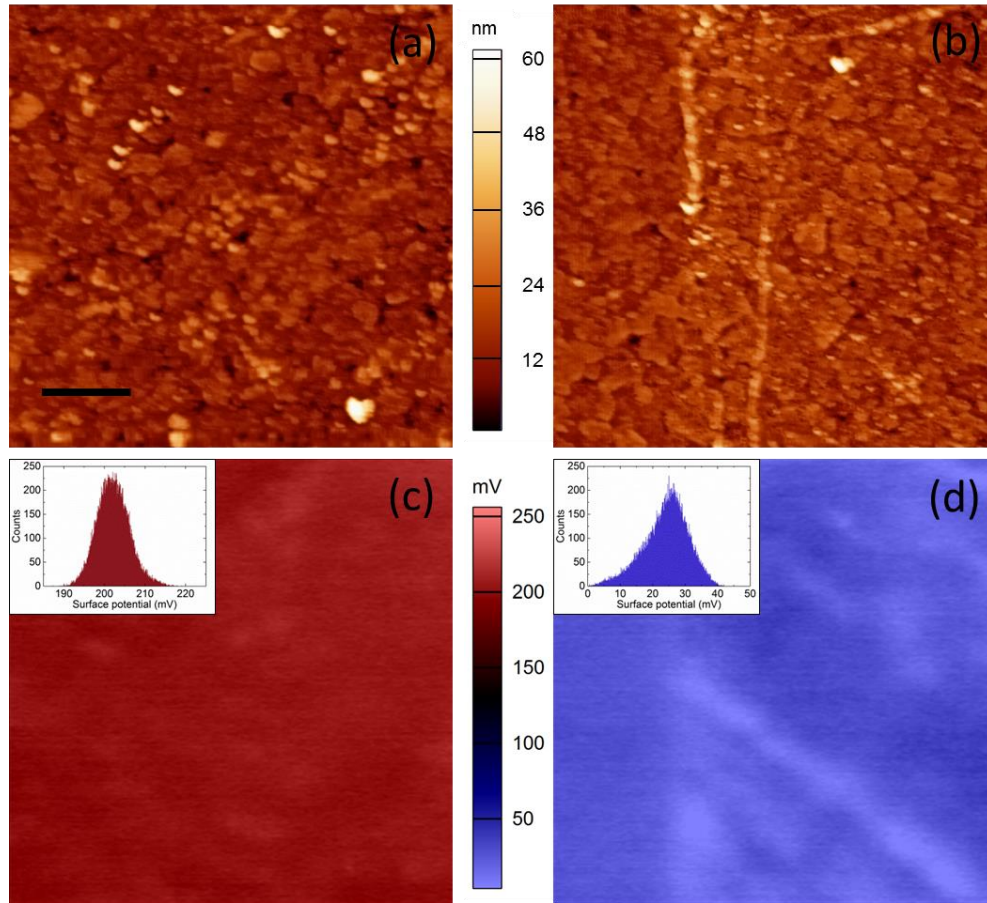


Figure 4 – AFM and KPFM analysis of glass/ITO (left panels) and glass/ITO/GBD (right panels) samples: (a, b) topography and (c, d) surface potential collected by KPFM on a typical region of $5 \times 5 \mu\text{m}$ (scale bar is $1 \mu\text{m}$). In the inset of (c) and (d) the histogram of the potential data from 4 regions are reported.

We measured the UV-vis absorption of the GBD and graphene films. The absorption measurements were taken after transferring the samples onto fused silica and onto glass/ITO substrates (Figure 5 and inset, respectively). The absorption spectrum of the graphene film (a semi-metal with zero bandgap - E_g) is dominated by a pronounced peak at $E=4.62 \text{ eV}$, which arises from strong electron-hole (excitonic) interactions (interband transitions from the bonding to the antibonding π -states) near the saddle-point singularity at the M-point of the Brillouin zone.

Instead, the GBD film has a less pronounced excitonic peak than graphene, but it shows an additional intense absorption feature in the UV region beyond 5 eV. In Figure 5 we derived the Tauc plot in the two cases. The Tauc plot uses spectrophotometric measures of the direct allowed transitions (*i.e.*, the photon absorption) and is typically employed to study the overall band structure of amorphous semiconductors and to evaluate their optical bandgap, which is altered by the presence of localized states with respect to their crystalline counterpart.⁵⁶ By calculating the intercept of the linear part of the curve with the x axis (photon energy), the optical gaps can be estimated. In case of graphene (1070°C) the intercept was not calculated since the excitonic peak dominates the absorption spectrum without any physical correspondence to an optical band gap (E_g): the intercept is expected to fall close to naught in spectral regions away from the exciton. However, this method can be applied to graphene oxide and functionalized graphene. In the former case, Mathkar et al.⁵⁷ confirmed the presence of an optical gap and showed the decrease of E_g towards zero which took place when reducing exfoliated graphene oxide to graphene: in a case where a far less pronounced exciton was observed with respect to the CVD grown material which is object of the present study. In the case of our GBD film (790°C), the absorption in the UV leads to an estimated optical gap E_g of about 5.1 eV. Several models predict the presence of a direct band gap in this range for the fully hydrogenated, sp^3 bonded GBD, *i.e.* graphane.¹⁹

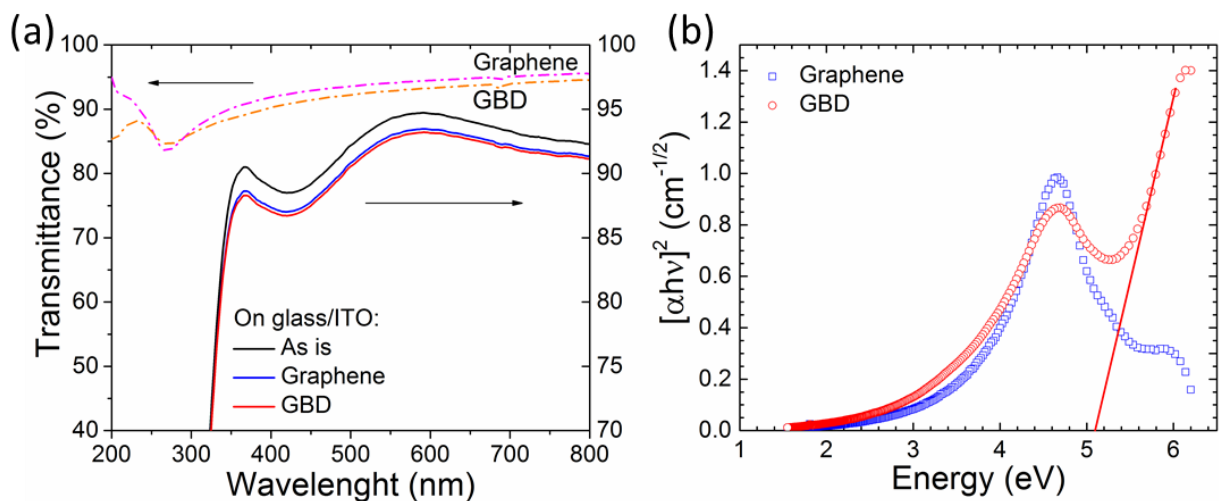


Figure 5 – Optical analysis of the CVD films. (a) Transmittance of graphene and GBD transferred on quartz substrates (top curves, left axis) and on glass/ITO substrates (bottom curves, right axis). (b) Tauc plot of graphene and GBD on quartz. The optical E_g value of GBD is extrapolated through a linear fit of the curve.

Sheet resistance measurements were taken by the four point probe method on the CVD samples transferred on Si/SiO₂. The GBD grown at 790/0/30' reported values in the range 215-400 kΩ/□. Reference graphene grown at 1070/10/10' has values in the order of 400-800 Ω/□. Therefore, when the temperature changes from 1070°C to 790°C, the sheet resistance of the film is found to have a remarkable increase of four orders of magnitude. This steep increase in sheet resistance is however consistent with the previous analyses: When lowering the CVD temperature, the amount of sp³ bonds (stabilized by “functional groups” such as hydrogen atoms) considerably increases at the expenses of the conductive sp² double bonds, rendering the GBD film almost electrically insulating.

2.2 Solar cells characterization

The current-voltage (I/V) plots of the fabricated solar cells under illumination (AM1.5G at 100 mW/cm^2) were measured. Figure 6a shows the I/V plots of cells made with GBD, PEDOT:PSS, and with no HTL as reference, respectively (under illumination). The photovoltaic characteristics of the devices are summarized in Table 2. The external quantum efficiency (EQE) of the cells is reported in Figure 6b. Figure 6c shows the energy levels of the layers composing the cell.

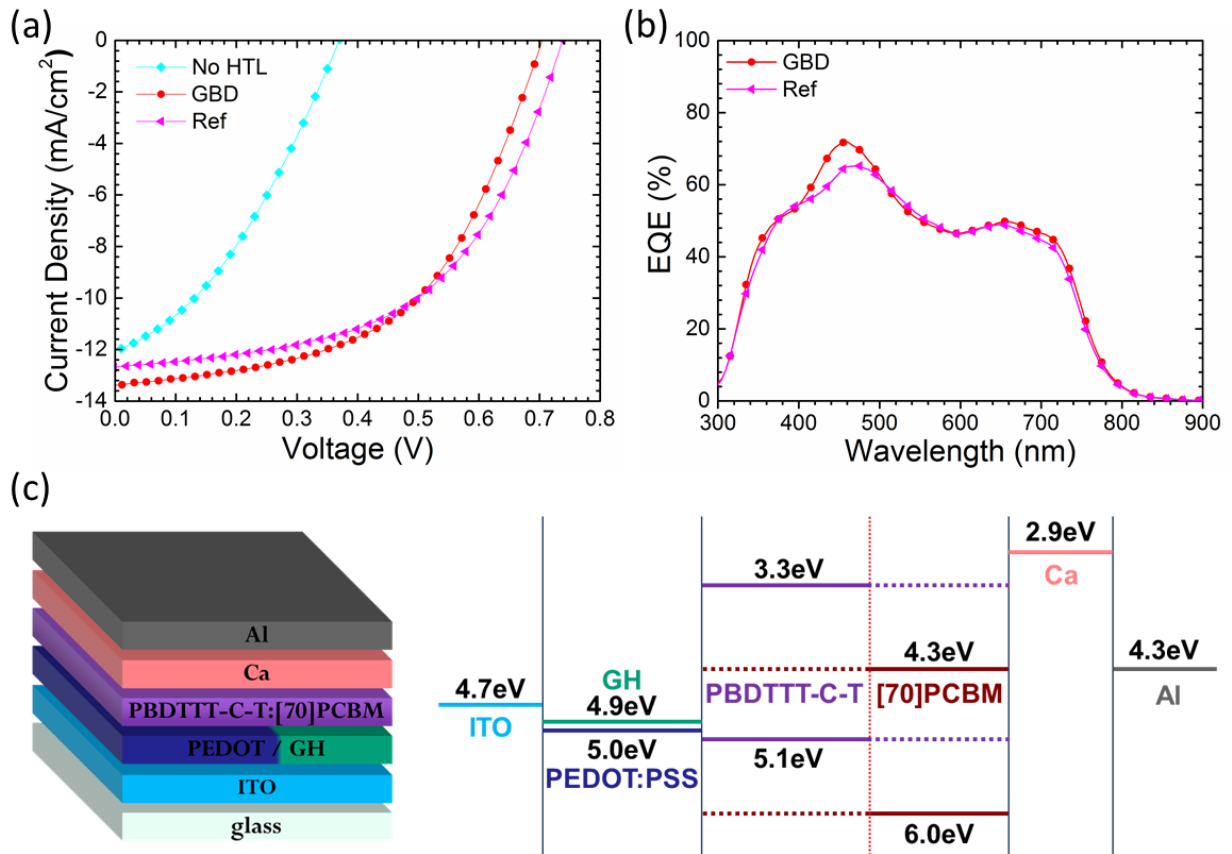


Figure 6 – (a) I/V curves under illumination of the devices with different HTLs. (b) EQE curves of best samples of GBD and Ref w/PEDOT:PSS. (c) Schematic (left) and energy level diagram (right) of the solar cells.

The cell with no HTL has low V_{OC} and FF (0.34 V and 38.4%, respectively), and reaches $\eta=1.7\%$. Such cell performance can be ascribed to an unbalanced energy level alignment between ITO and the HOMO of PBDTTT-C-T (giving rise to an energy barrier of ~ 0.4 eV, see Figure 6c)⁵⁸ and to the occurrence of charge recombination (due to inefficient hole collection at the anode). The insertion of GBD between ITO and the PBDTTT-C-T layer brings the cell to $\eta=5\%$. This steep improvement in η is given by the increase in both V_{OC} (0.71 V) and FF (52.5%). For comparison, the reference cell made with PEDOT:PSS as HTL has the same efficiency ($\sim 5\%$) and analogous photovoltaic parameters (see Table 1). The GBD is thus able to provide an optimal energy level alignment at the anode, as much as PEDOT:PSS does. This is remarkable considering the latter material was proposed years ago and since then has gone through various stages of optimization which made it the state-of-the-art HTL in OSC. Further, the best GBD device shows an even higher J_{SC} than the PEDOT:PSS one (~ 13.4 vs 12.7 mA/cm²), likely due to the atomic thickness of the GBD film that eases the charge collection at the anode via quantum tunneling through the HTL. The PEDOT:PSS is instead ~ 40 nm thick, and in this case a portion of the travelling holes might be lost because of charge recombination. The EQE curves (Figure 6b) of the two cells are identical except for the range 400÷500nm, where the GBD cell exhibits a higher quantum efficiency than the reference cell, with a slight shift of the main peak from 470 to 460nm, giving account to the higher J_{sc} measured in the I/V tests (Table 2).

Table 2 – Average and max values of the electrical parameters of the fabricated solar cells.

Hole Transport Layer (HTL)	Voc (V)		Jsc (mA/cm ²)		FF (%)		Eff (%)		R (Ω·cm ²)	
	<i>Avg</i>	<i>Max</i>	<i>Avg</i>	<i>Max</i>	<i>Avg</i>	<i>Max</i>	<i>Avg</i>	<i>Max</i>	<i>Rs</i>	<i>Rsh</i>
GBD (790°C_1L)	0.630	0.712	-11.08	-13.38	48.67	52.54	3.43	5.01	14.2	575
GBD (790°C_2L)	0.662	0.669	-5.14	-5.85	39.95	39.74	1.36	1.56	29.8	319
Graphene (1070°C)	0.316	0.439	-6.56	-7.31	28.69	34.12	0.60	1.09	102	30.8
Ref PEDOT:PSS	0.734	0.738	-12.51	-12.69	52.52	53.46	4.82	5.00	13.2	616
No HTL	0.341	0.352	-12.36	-12.70	36.98	38.43	1.56	1.72	17.1	105

We further investigated the effect of GBD thickness on the cell performance, making cells with one and two GBD films (see Experimental section). The results are reported in Fig. 7, along with a further comparison with a cell made with pristine graphene as HTL. The comparison between cells made with graphene and GBD is very informative. The cell with graphene attains a η of 1.1% that is ascribable to a steep decrease in Voc and FF (0.31 vs 0.66 V and 28.7% vs 48.7%, respectively).

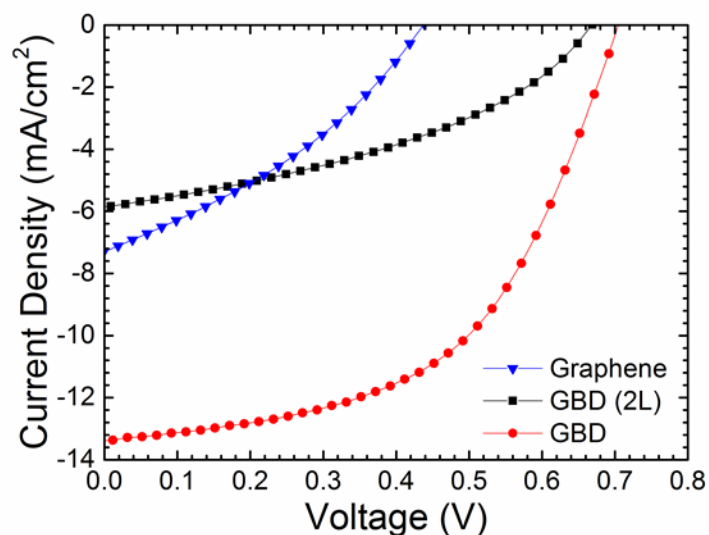


Figure 7 – I/V curves under illumination of the devices with graphene, GBD and two GBD films as HTLs.

These results can be explained considering the properties of the CVD graphene layer. Being it highly conductive ($R_s \sim 400 \Omega/\square$) but with a work function of ~ 4.6 eV, CVD graphene can work as transparent conductor and as metallic electrode in Schottky barrier solar cells.⁵⁹ However, these properties hinder its use as HTL since the electron flow is not blocked but instead there could be an alignment with the LUMO of [70]PCBM (see Figure 6c) lying at ~ 4.3 eV, giving rise to charge recombination. In the case of GBD, the graphene structure is modified by the insertion of sp^3 groups in the lattice (which appear to be hydrogen-terminated). This increases the work function level to ~ 4.9 eV as found by KFPM, making the material hole-selecting. The effect of the double layer on the cell's I/V seems to confirm the properties of the GBD film that make it an efficient HTL. In this case the V_{OC} remains quite stable with respect to the reference cell, while J_{SC} and FF both significantly decrease, bringing the η to 1.5%. The stability of the V_{OC} can be explained by the work function of the double GBD layer, which has the same value of the single layer. Instead, the effect of the increased layer thickness on the charge collection

negatively reflects in the J_{SC} of cell made with two GBD films, which is halved. However, a detrimental effect on the J_{SC} due to the transfer process of two layers can be also envisaged in this respect. Nevertheless, the J_{SC} dependence on thickness is consistent with what previously reported in the case of graphene⁶⁰ and graphene oxide.³²

CONCLUSION

In conclusion, our work demonstrates that the CVD of graphene from ethanol vapor in specific conditions can give rise to the growth of GBDs having different properties from pristine graphene. We investigated a range of temperature below 1000°C, demonstrating the growth of a sp^3 -rich GBD film at 790°C. The GBD film has atomic thickness and exhibits a large optical gap and almost electrically insulating properties. We tested the GBD as hole transport layer in organic solar cells, reaching the performances of state-of-the-art cells made with standard PEDOT:PSS. Further work on GBD films for organic photovoltaics are in order to further increase the cell performance and also evaluate the lifetime stability, which is expected to be extended considering that the GBD would not corrode the ITO electrode (a known issue related to the use of PEDOT:PSS). Moreover, our findings can lead to the development of a rather large class of novel GBDs produced by the direct catalytic CVD growth on metal substrates. We demonstrated that by lowering the growth temperature, functional groups can be inserted at equilibrium into growing carbonaceous films structurally related to graphene. In this scenario, by using appropriate precursors and conditions it will be possible to tailor the functional properties of the GBDs for desired applications. Such process presents several advantages with respect to post-growth treatments and is also compatible with the fabrication of devices via solution processing.

EXPERIMENTAL

Growth of graphene and graphene-based derivative (GBD) films

The films were grown by ethanol-CVD on Cu foils (25 μ m thick, 99.95 purity) at low-pressure (4 mbar). The CVD system was made of a quartz tube (2m long) coaxial to a furnace, fitted with vacuum pumps (rotary vane and turbo-molecular pump), a digitally-controlled gas/vapor feed system and a quartz sled sample holder. For pristine graphene, the Cu foils were annealed for 20 min at 1070°C while flowing Ar/H₂ (20/20 sccm).^{34, 38, 61} After annealing, the growth was performed at 1070°C by bubbling ethanol in the chamber (0.1% in Ar/H₂ as carrier gas at 20/10 sccm). For the GBD, the Cu foils were annealed for 20 min at 790°C while flowing Ar/H₂ (20/20 sccm). After annealing, the growth was performed at 790°C by bubbling ethanol in the chamber (0.1% in Ar as carrier gas at 20 sccm). In both cases, just after the growth the Cu foils were extracted from the hot zone for a rapid cooling.

Film transfer

After the CVD process, the Cu foils were protected with cyclododecane⁶² and then etched away in an ammonium persulphate or nitric acid bath (70% nitric acid diluted in distilled water, 1:3) at ambient temperature for three hours. After the etching, the floating films were scooped with a clean Si/SiO₂ substrate and transferred into distilled water for rinsing. The films were finally scooped from the rinsing bath with Si/SiO₂ and quartz substrates for the characterizations. In the same way, the graphene and GBD films were transferred onto glass/ITO substrates for the solar cells fabrication. In the case of the GBD-2L, the film transfer was repeated twice.

Raman spectroscopy

A Ramanor U1000 with double monochromator and an electrically-cooled Hamamatsu R943-02 photomultiplier for photon-counting detection was used for Raman spectroscopy analysis.

The laser beam (Ar^+ , 514.5 nm) was focused to a diameter of approximately 1 μm , taking care of minimizing surface heating (power below 1 mW).

Transmission electron microscopy

TEM characterization was performed using a Tecnai F20 microscope, operated at 120kV to reduce the radiation damage to graphene crystals.

Absorption spectroscopy

Optical transmittance spectra of the films transferred on quartz and glass/ITO were acquired with a UV-VIS-NIR spectrophotometer (Shimadzu UV2550).

X-ray photoemission spectroscopy

X-ray photoelectron spectroscopy (XPS) measurements were carried out with a VG Escalab MkII Spectrometer on the as-grown copper foils, few minutes after the CVD growth. The XPS chamber is equipped with oil-free pumps to avoid carbon contaminations (an Ag reference sample was analyzed before revealing no carbon signal).

Kelvin Probe Microscopy (KPM)

We performed Kelvin Probe Force Microscopy (KPFM) measurements on the GBD film deposited on glass/ITO and on a glass/ITO reference sample. The measurements were taken in ambient conditions with an Asylum Research MFP3D AFM using a Pt/Ir-coated silicon tips with radius of curvature $R=20\text{-}30$ nm, quality factor $Q=150$ and spring constant $k=0.65\text{-}1$ N/m. The measurements were done with the same tip to avoid changes due to ambient tip condition, temperature and humidity. The following formula was used to devise the work function of the samples from the measured surface potential (V_{CPD}):

$$V_{\text{CPD}} = \frac{\Phi_{\text{tip}} - \Phi_{\text{sample}}}{-e}$$

Electrical measurements

The electrical sheet resistance of the films transferred onto Si/SiO₂ was with a four point probe system with four fixed, collinear WC tips (spaced overall by 3 mm) connected to a current source and a low-voltage meter. The measurements were taken multiple times over an area of at least 5×5 mm² on each sample and then averaged.

Solar cell fabrication

Polymer bulk-heterojunction solar cells were fabricated onto glass/ITO substrates (Kintec, 15Ω/□). A low-band gap polymer (PBDTTT-CT), previously reported in PSCs with up to 8% of efficiency, was used.⁶³ The cells were fabricated with the so-called “direct” architecture, the most suitable to compare the performance and stability of the GBD as HTL to those of PEDOT:PSS.^{18, 64} The glass/ITO substrates were patterned by wet etching using an aqueous solution of hydrobromic acid and cleaned by ultrasonic bath cycles in detergent, deionized water, acetone, and ethanol (10 min for each step). Graphene and GBD films were deposited onto glass/ITO substrates as HTL as described above. As reference, solar cells were also fabricated with PEDOT:PSS (VPAI 4083, purchased as aqueous dispersion from Heraeus) as HTL. PEDOT:PSS was spin-coated in a glove box at 5000rpm for 60s and then dried by thermal annealing at 150°C for 10 min in a nitrogen atmosphere. To prepare the photoactive blend, PBDTTT-C-T (Solarmer) and [70]PCBM (Solenne BV) blends (1:1.5) were dissolved in ortho-xylene at 2.5 wt% and stirred on a hot plate at 50°C for 16h. PBDTTT-C-T:[70]PCBM was spin-coated at 1000rpm for 60s, then vacuum-dried for 20min to remove residual DIO from the film. Diiodooctane (DIO) was added to the blend solution (5% v/v) to improve the morphology of the film during deposition. The solar cells were completed by thermally evaporating 10 nm of Ca

(0.5Å/s) and 100 nm of Al (1.5Å/s) in high vacuum ($\sim 10^{-6}$ mbar). Shadow masks were applied to define a 10mm² active area for each device. 16 cells were fabricated for each kind of tested HTL.

Solar cell characterization

A custom-made system comprising a sourcemeter (Keithley 2612) and a mono-chromator (Newport 74000) was used to measure the external quantum efficiency (EQE) of the solar cells. I/V curves of the cells under a class A solar simulator (ABET Technologies Sun2000) were recorded. The irradiation level of 1sun (100mW/cm²) AM1.5G standard at the height and position of the solar cell was verified with a calibrated pyranometer (Skye SKS1110). All the cells were measured unsealed and covered with a shadow mask to avoid measurement inaccuracies.

AUTHOR INFORMATION

Corresponding Author

*E-mail: andrea.capasso@iit.it (Andrea Capasso).

Author Contributions

The manuscript was written through contributions of all authors. All authors have given approval to the final version of the manuscript.

References

1. Green, M. A.; Emery, K.; Hishikawa, Y.; Warta, W.; Dunlop, E. D., Solar Cell Efficiency Tables (version 46). *Prog. Photovoltaics* **2015**, *23* (7), 805-812.
2. Espinosa, N.; Hösel, M.; Angmo, D.; Krebs, F. C., Solar Cells with One-day Energy Payback for the Factories of the Future. *Energy Environ. Science* **2012**, *5* (1), 5117-5117.
3. Reichelstein, S.; Yorston, M., The Prospects For Cost Competitive Solar PV Power. *Energy Policy* **2013**, *55*, 117-127.
4. Zhao, J.; Li, Y.; Yang, G.; Jiang, K.; Lin, H.; Ade, H.; Ma, W.; Yan, H., Efficient Organic Solar Cells Processed from Hydrocarbon Solvents. *Nature Energy* **2016**, *1*, 15027.
5. Machui, F.; Hösel, M.; Li, N.; Spyropoulos, G. D.; Ameri, T.; Sondergaard, R. R.; Jorgensen, M.; Scheel, A.; Gaiser, D.; Kreul, K.; Lenssen, D.; Legros, M.; Lemaitre, N.;

- Vilkman, M.; Valimaki, M.; Nordman, S.; Brabec, C. J.; Krebs, F. C., Cost Analysis of Roll-to-roll Fabricated ITO Free Single and Tandem Organic Solar Modules Based on Data from Manufacture. *Energy Environ. Sci.* **2014**, *7*, 2792-2802.
6. Capasso, A.; Salamandra, L.; Di Carlo, A.; Bell, J. M.; Motta, N., Low-temperature Synthesis of Carbon Nanotubes on Indium Tin Oxide Electrodes for Organic Solar Cells. *Beilstein J. Nanotech.* **2012**, *3* (1), 524-532.
 7. Capasso, A.; Salamandra, L.; Chou, A.; Di Carlo, A.; Motta, N., Multi-wall Carbon Nanotube Coating of Fluorine-doped Tin Oxide as an Electrode Surface Modifier for Polymer Solar Cells. *Sol. Energy Mater. Sol. Cells* **2014**, *122*, 297-302.
 8. Krebs, F. C.; Tromholt, T.; Jorgensen, M., Upscaling of Polymer Solar Cell Fabrication Using Full Roll-to-roll Processing. *Nanoscale* **2010**, *2* (6), 873-886.
 9. Søndergaard, R.; Hösel, M.; Angmo, D.; Larsen-Olsen, T. T.; Krebs, F. C., Roll-to-roll Fabrication of Polymer Solar Cells. *Mater. Today* **2012**, *15* (1-2), 36-49.
 10. Darling, S. B.; You, F., The Case for Organic Photovoltaics. *RSC Adv.* **2013**, *3* (39), 17633-17648.
 11. Chen, C.-C.; Chang, W.-H.; Yoshimura, K.; Ohya, K.; You, J.; Gao, J.; Hong, Z.; Yang, Y., An Efficient Triple-Junction Polymer Solar Cell Having a Power Conversion Efficiency Exceeding 11%. *Adv. Mater.* **2014**, *26* (32), 5670-5677.
 12. Yusoff, A. R. B. M.; Kim, D.; Kim, H. P.; Shneider, F. K.; da Silva, W. J.; Jang, J., A High Efficiency Solution Processed Polymer Inverted Triple-junction Solar Cell Exhibiting a Power Conversion Efficiency of 11.83%. *Energy Environ. Sci.* **2015**, *8* (1), 303-316.
 13. Zhou, H.; Zhang, Y.; Mai, C.-K.; Collins, S. D.; Bazan, G. C.; Nguyen, T.-Q.; Heeger, A. J., Polymer Homo-Tandem Solar Cells with Best Efficiency of 11.3%. *Adv. Mater.* **2015**, *27* (10), 1767-1773.
 14. Zampetti, A.; Fallahpour, A. H.; Dianetti, M.; Salamandra, L.; Santoni, F.; Gagliardi, A.; Auf der Maur, M.; Brunetti, F.; Reale, A.; Brown, T. M.; Di Carlo, A., Influence of the Interface Material Layers and Semiconductor Energetic Disorder on the Open Circuit Voltage in Polymer Solar Cells. *J. Polym. Sci., Part B: Polym. Phys.* **2015**, *53* (10), 690-699.
 15. Dou, L.; You, J.; Hong, Z.; Xu, Z.; Li, G.; Street, R. A.; Yang, Y., 25th Anniversary Article: A Decade of Organic/Polymeric Photovoltaic Research. *Adv. Mater.* **2013**, *25* (46), 6642-6671.
 16. Lattante, S., Electron and Hole Transport Layers: Their Use in Inverted Bulk Heterojunction Polymer Solar Cells. *Electronics* **2014**, *3* (1), 132.
 17. Derouiche, H.; Djara, V., Impact of the Energy Difference in LUMO and HOMO of the Bulk Heterojunctions Components on the Efficiency of Organic Solar Cells. *Sol. Energy Mater. Sol. Cells* **2007**, *91* (13), 1163-1167.
 18. Jørgensen, M.; Norrman, K.; Gevorgyan, S. A.; Tromholt, T.; Andreasen, B.; Krebs, F. C., Stability of Polymer Solar Cells. *Adv. Mater.* **2012**, *24* (5), 580-612.
 19. Elias, D. C.; Nair, R. R.; Mohiuddin, T. M. G.; Morozov, S. V.; Blake, P.; Halsall, M. P.; Ferrari, A. C.; Boukhalov, D. W.; Katsnelson, M. I.; Geim, A. K.; Novoselov, K. S., Control of Graphene's Properties by Reversible Hydrogenation: Evidence for Graphane. *Science* **2009**, *323* (5914), 610-613.
 20. Nair, R. R.; Ren, W.; Jalil, R.; Riaz, I.; Kravets, V. G.; Britnell, L.; Blake, P.; Schedin, F.; Mayorov, A. S.; Yuan, S.; Katsnelson, M. I.; Cheng, H.-M.; Strupinski, W.; Bulusheva, L. G.; Okotrub, A. V.; Grigorieva, I. V.; Grigorenko, A. N.; Novoselov, K. S.; Geim, A. K., Fluorographene: A Two-Dimensional Counterpart of Teflon. *Small* **2010**, *6* (24), 2877-2884.

21. Wang, L.; Sun, Y. Y.; Lee, K.; West, D.; Chen, Z. F.; Zhao, J. J.; Zhang, S. B., Stability of Graphene Oxide Phases from First-principles Calculations. *Phys. Rev. B* **2010**, *82* (16), 161406.
22. Chen, Y.; Lin, W.-C.; Liu, J.; Dai, L., Graphene Oxide-Based Carbon Interconnecting Layer for Polymer Tandem Solar Cells. *Nano Letters* **2014**, *14* (3), 1467-1471.
23. Gao, L.; Ni, G.-X.; Liu, Y.; Liu, B.; Castro Neto, A. H.; Loh, K. P., Face-to-face Transfer of Wafer-scale Graphene Films. *Nature* **2013**, *505* (7482), 190-194.
24. Iwan, A.; Chuchmała, A., Perspectives of Applied Graphene: Polymer Solar Cells. *Prog. Polym. Sci.* **2012**, *37* (12), 1805-1828.
25. Liu, Z.; Li, J.; Sun, Z.-H.; Tai, G.; Lau, S.-P.; Yan, F., The Application of Highly Doped Single-Layer Graphene as the Top Electrodes of Semitransparent Organic Solar Cells. *ACS Nano* **2012**, *6* (1), 810-818.
26. Sun, Y.; Zhang, W.; Chi, H.; Liu, Y.; Hou, C. L.; Fang, D., Recent Development of Graphene Materials Applied in Polymer Solar Cell. *Renewable Sustainable Energy Rev.* **2015**, *43*, 973-980.
27. Wu, J.; Becerril, H. a.; Bao, Z.; Liu, Z.; Chen, Y.; Peumans, P., Organic Solar Cells with Solution-processed Graphene Transparent Electrodes. *Appl. Phys. Lett.* **2008**, *92* (26), 263302-263302.
28. Manzano-Ramírez, A.; López-Naranjo, E. J.; Soboyejo, W.; Meas-Vong, Y.; Vilquin, B., A Review on the Efficiency of Graphene-Based BHJ Organic Solar Cells. *J. Nanomat.* **2015**, *2015*.
29. Kim, H.; Byun, J.; Bae, S.-H.; Ahmed, T.; Zhu, J.-X.; Kwon, S.-J.; Lee, Y.; Min, S.-Y.; Wolf, C.; Seo, H.-K.; Ahn, J.-H.; Lee, T.-W., On-Fabrication Solid-State N-Doping of Graphene by an Electron-Transporting Metal Oxide Layer for Efficient Inverted Organic Solar Cells. *Adv. En. Mater.* **2016**, *6* (12), n/a-n/a.
30. Huang, J.; Carpenter, J. H.; Li, C.-Z.; Yu, J.-S.; Ade, H.; Jen, A. K. Y., Highly Efficient Organic Solar Cells with Improved Vertical Donor–Acceptor Compositional Gradient Via an Inverted Off-Center Spinning Method. *Adv. Mater.* **2016**, *28* (5), 967-974.
31. Liu, J.; Durstock, M.; Dai, L., Graphene Oxide Derivatives as Hole- and Electron-extraction Layers for High-performance Polymer Solar Cells. *Energy Environ. Sci.* **2014**, *7* (4), 1297-1306.
32. Li, S.-S.; Tu, K.-H.; Lin, C.-C.; Chen, C.-W.; Chhowalla, M., Solution-Processable Graphene Oxide as an Efficient Hole Transport Layer in Polymer Solar Cells. *ACS Nano* **2010**, *4* (6), 3169-3174.
33. Wang, Y.; Xu, X.; Lu, J.; Lin, M.; Bao, Q.; Özyilmaz, B.; Loh, K. P., Toward High Throughput Interconvertible Graphane-to-Graphene Growth and Patterning. *ACS Nano* **2010**, *4* (10), 6146-6152.
34. Capasso, A.; Dikonimos, T.; Sarto, F.; Tamburrano, A.; De Bellis, G.; Sarto, M. S.; Faggio, G.; Malara, A.; Messina, G.; Lisi, N., Nitrogen-doped Graphene Films from Chemical Vapor Deposition of Pyridine: Influence of Process Parameters on the Electrical and Optical Properties. *Beilstein J. Nanotech.* **2015**, *6*, 2028-2038.
35. Paul, R. K.; Badhulika, S.; Niyogi, S.; Haddon, R. C.; Boddu, V. M.; Costales-Nieves, C.; Bozhilov, K. N.; Mulchandani, A., The Production of Oxygenated Polycrystalline Graphene by One-step Ethanol-chemical Vapor Deposition. *Carbon* **2011**, *49* (12), 3789-3795.

36. Ivan, V.; Sergei, S.; Iliia, I.; Pasquale, F. F.; Sheng, D.; Harry, M.; Miaofang, C.; Dale, H.; Panos, D.; Nickolay, V. L., Electrical and Thermal Conductivity of Low Temperature CVD Graphene: the Effect of Disorder. *Nanotechnology* **2011**, *22* (27), 275716.
37. Tuinstra, F.; Koenig, J. L., Raman Spectrum of Graphite. *J. Chem. Phys.* **1970**, *53* (3), 1126-1130.
38. Faggio, G.; Capasso, A.; Messina, G.; Santangelo, S.; Dikonimos, T.; Gagliardi, S.; Giorgi, R.; Morandi, V.; Ortolani, L.; Lisi, N., High-temperature Growth of Graphene Films on Copper Foils by Ethanol Chemical Vapor Deposition. *J. Phys. Chem. C* **2013**, *117* (41), 21569-21576.
39. Meyer, J. C.; Geim, A. K.; Katsnelson, M. I.; Novoselov, K. S.; Booth, T. J.; Roth, S., The Structure of Suspended Graphene Sheets. *Nature* **2007**, *446* (7131), 60-63.
40. Dong, X.; Wang, P.; Fang, W.; Su, C.-Y.; Chen, Y.-H.; Li, L.-J.; Huang, W.; Chen, P., Growth of Large-sized Graphene Thin-films by Liquid Precursor-based Chemical Vapor Deposition Under Atmospheric Pressure. *Carbon* **2011**, *49* (11), 3672-3678.
41. Santangelo, S.; Messina, G.; Malara, A.; Lisi, N.; Dikonimos, T.; Capasso, A.; Ortolani, L.; Morandi, V.; Faggio, G., Taguchi optimized synthesis of graphene films by copper catalyzed ethanol decomposition. *Diam. Rel. Mater.* **2014**, *41*, 73-78.
42. Ferrari, A. C.; Meyer, J. C.; Scardaci, V.; Casiraghi, C.; Lazzeri, M.; Mauri, F.; Piscanec, S.; Jiang, D.; Novoselov, K. S.; Roth, S.; Geim, A. K., Raman Spectrum of Graphene and Graphene Layers. *Phys. Rev. Lett.* **2006**, *97* (18), 187401.
43. Malard, L. M.; Pimenta, M. A.; Dresselhaus, G.; Dresselhaus, M. S., Raman Spectroscopy in Graphene. *Phys. Rep.* **2009**, *473* (5-6), 51-87.
44. Lisi, N.; Buonocore, F.; Dikonimos, T.; Leoni, E.; Faggio, G.; Messina, G.; Morandi, V.; Ortolani, L.; Capasso, A., Rapid and Highly Efficient Growth of Graphene on Copper by Chemical Vapor Deposition of Ethanol. *Thin Solid Films* **2014**, *571* (P1), 139-144.
45. Cançado, L. G.; Takai, K.; Enoki, T.; Endo, M.; Kim, Y. A.; Mizusaki, H.; Jorio, A.; Coelho, L. N.; Magalhães-Paniago, R.; Pimenta, M. A., General Equation for the Determination of the Crystallite Size L_a of Nanographite by Raman Spectroscopy. *Appl. Phys. Lett.* **2006**, *88* (16), 163106.
46. Ferrari, A. C., Raman Spectroscopy of Graphene and Graphite: Disorder, Electron-phonon Coupling, Doping and Nonadiabatic Effects. *Sol. State Comm.* **2007**, *143* (1-2), 47-57.
47. Eckmann, A.; Felten, A.; Mishchenko, A.; Britnell, L.; Krupke, R.; Novoselov, K. S.; Casiraghi, C., Probing the Nature of Defects in Graphene by Raman Spectroscopy. *Nano Letters* **2012**, *12* (8), 3925-3930.
48. Eckmann, A.; Felten, A.; Verzhbitskiy, I.; Davey, R.; Casiraghi, C., Raman Study on Defective Graphene: Effect of the Excitation Energy, Type, and Amount of Defects. *Phys. Rev. B* **2013**, *88* (3), 035426.
49. Cançado, L. G.; Jorio, A.; Ferreira, E. H. M.; Stavale, F.; Achete, C. A.; Capaz, R. B.; Moutinho, M. V. O.; Lombardo, A.; Kulmala, T. S.; Ferrari, A. C., Quantifying Defects in Graphene via Raman Spectroscopy at Different Excitation Energies. *Nano Letters* **2011**, *11* (8), 3190-3196.
50. Seifert, M.; Vargas, J. E. B.; Bobinger, M.; Sachsenhauser, M.; Cummings, A. W.; Roche, S.; Garrido, J. A., Role of Grain Boundaries in Tailoring Electronic Properties of Polycrystalline Graphene by Chemical Functionalization. *2D Mater.* **2015**, *2* (2), 024008.
51. Chu, P. K.; Li, L. H., Characterization of Amorphous and Nanocrystalline Carbon Films. *Mater. Chem. Phys.* **2006**, *96* (2-3), 253-277.

52. Luo, Z.; Yu, T.; Kim, K.-j.; Ni, Z.; You, Y.; Lim, S.; Shen, Z.; Wang, S.; Lin, J., Thickness-Dependent Reversible Hydrogenation of Graphene Layers. *ACS Nano* **2009**, *3* (7), 1781-1788.
53. Teng, C.-C.; Ma, C.-C. M.; Lu, C.-H.; Yang, S.-Y.; Lee, S.-H.; Hsiao, M.-C.; Yen, M.-Y.; Chiou, K.-C.; Lee, T.-M., Thermal Conductivity and Structure of Non-covalent Functionalized Graphene/epoxy Composites. *Carbon* **2011**, *49* (15), 5107-5116.
54. Lascovich, J. C.; Giorgi, R.; Scaglione, S., Evaluation of the sp²/sp³ Ratio in Amorphous Carbon Structure by XPS and XAES. *Appl. Surf. Sci.* **1991**, *47* (1), 17-21.
55. Shi, Y.; Kim, K. K.; Reina, A.; Hofmann, M.; Li, L.-J.; Kong, J., Work Function Engineering of Graphene Electrode via Chemical Doping. *ACS Nano* **2010**, *4* (5), 2689-2694.
56. Tauc, J., Optical Properties and Electronic Structure of Amorphous Ge and Si. *Mater. Res. Bull.* **1968**, *3* (1), 37-46.
57. Mathkar, A.; Tozier, D.; Cox, P.; Ong, P.; Galande, C.; Balakrishnan, K.; Leela Mohana Reddy, A.; Ajayan, P. M., Controlled, Stepwise Reduction and Band Gap Manipulation of Graphene Oxide. *J. Phys. Chem. Lett.* **2012**, *3* (8), 986-991.
58. Huo, L.; Zhang, S.; Guo, X.; Xu, F.; Li, Y.; Hou, J., Replacing Alkoxy Groups with Alkylthienyl Groups: A Feasible Approach To Improve the Properties of Photovoltaic Polymers. *Angew. Chem., Int. Ed.* **2011**, *50* (41), 9697-9702.
59. Lancellotti, L.; Bobeico, E.; Capasso, A.; Lago, E.; Delli Veneri, P.; Leoni, E.; Buonocore, F.; Lisi, N., Combined Effect of Double Antireflection Coating and Reversible Molecular Doping on Performance of Few-layer Graphene/n-silicon Schottky Barrier Solar Cells. *Sol. Energy* **2016**, *127*, 198-205.
60. You, P.; Liu, Z.; Tai, Q.; Liu, S.; Yan, F., Efficient Semitransparent Perovskite Solar Cells with Graphene Electrodes. *Adv. Mater.* **2015**, *27* (24), 3632-3638.
61. Asif, M.; Tan, Y.; Pan, L.; Li, J.; Rashad, M.; Usman, M., Thickness Controlled Water Vapors Assisted Growth of Multilayer Graphene by Ambient Pressure Chemical Vapor Deposition. *J. Phys. Chem. C* **2015**, *119* (6), 3079-3089.
62. Capasso, A.; De Francesco, M.; Leoni, E.; Dikonimos, T.; Buonocore, F.; Lancellotti, L.; Bobeico, E.; Sarto, M. S.; Tamburrano, A.; De Bellis, G.; Lisi, N., Cyclododecane as Support Material for Clean and Facile Transfer of Large-area Few-layer Graphene. *Appl. Phys. Lett.* **2014**, *105* (11).
63. La Notte, L.; Polino, G.; Ciceroni, C.; Brunetti, F.; Brown, T. M.; Di Carlo, A.; Reale, A., Spray-Coated Polymer Solar Cells based on Low-Band-Gap Donors Processed with ortho -Xylene. *Energy Technol.* **2014**, *2* (9-10), n/a-n/a.
64. Etxebarria, I.; Guerrero, A.; Albero, J.; Garcia-Belmonte, G.; Palomares, E.; Pacios, R., Inverted vs Standard PTB7:PC70BM Organic Photovoltaic Devices. The Benefit of Highly Selective and Extracting Contacts in Device Performance. *Org. Electron.* **2014**, *15* (11), 2756-2762.